Biomaterials 30 (2009) 3946–3955

Contents lists available at ScienceDirect

Biomaterials

journal homepage: www.elsevier.com/locate/biomaterials

# Self-assembly of pH-responsive fluorinated dendrimer-based particulates for drug delivery and noninvasive imaging

Jason M. Criscione [a], Bonaire L. Le [b], Eric Stern [a], Matthew Brennan [c], Christoph Rahner [d], Xenophon Papademetris [a,e], Tarek M. Fahmy [a,b,*]

[a] Malone Engineering Center, 55 Prospect Street, New Haven, CT 06511, USA
[b] Department of Chemical Engineering, Yale University, New Haven, CT 06511, USA
[c] Department of Surgery, Yale University, New Haven, CT 06520, USA
[d] Department of Cell Biology, Yale University, New Haven, CT 06520, USA
[e] Department of Diagnostic Radiology, Yale University, New Haven, CT 06520, USA

ARTICLE INFO

*Article history:*
Received 30 January 2009
Accepted 13 April 2009
Available online 13 May 2009

*Keywords:*
PAMAM
Fluorinated dendrimers
pH-responsive
$^{19}$F MRI
Self-assembly

ABSTRACT

Dendrimers are nanoscale macromolecules with well-defined branching chemical structures. Control over the architecture and function of these structures has enabled many advances in materials science and biomedical applications. Though dendrimers are directly synthesized by iteration of simple repetitive steps, generation of the larger, more complex structures required for many biomedical applications by covalent synthetic methods has been challenging. Here we demonstrate a spontaneous self-assembly of poly(amidoamine) dendrimers into complex nanoscopic and microscopic particulates following partial fluorination of the constituent dendrimer subunits. These dense particulates exhibit a stimulus-induced response to low external pH that causes their disassembly over time, enabling controlled release of encapsulated agents. In addition, we show that these assemblies offer a sufficiently high density of fluorine spins to enable detection of their site-specific accumulation *in vivo* by $^{19}$F magnetic resonance imaging ($^{19}$F MRI). Fluorinated dendrimer-based particulates present new features and capabilities important for a wide variety of emerging biomedical applications.



## 1. Introduction

Dendrimers are a class of branched polymers distinguished by their repeating patterns emanating from a central core [1]. The well-defined architecture of these molecules obtained by control over their synthesis [2] has led to a diverse array of therapeutic and diagnostic applications [3–15]. Though dendrimers are directly synthesized by iteration of simple repetitive steps, generation of larger and more complex structures by covalent synthetic methods has proven far more challenging and expensive. Thus, assembling dendrimer or dendron subunits, either by self-assembly [16–18] or directed assembly [19–24], has become an attractive and inexpensive short cut to achieve these structures. However, fabrication of ordered, solid particulates from dendrimers for applications in materials science and biological systems has not been reported to date.

We hypothesized that controlled fluorination of poly(amidoamine) (PAMAM) starburst dendrimers would mediate self-assembly through the "fluorophobic effect" [17,18,25]. This effect—the tendency of fluorinated molecules to separate and assemble into a fluorous phase that is both hydrophobic and lipophobic [25] has unveiled a unique set of non-covalent interactions useful for engineering self-assembled systems. Exerting control over these interactions will enable the design of interesting new systems for therapeutic and diagnostic applications. Indeed, this effect has been observed in the self-assembly of semi-fluorinated monodendrons into supramolecular columnar dendrimers which exhibit liquid crystalline properties [17,18].

We chose PAMAM starburst dendrimers as our starting subunit because of their well-established properties and wide use in biomedical applications [1]. Additionally, the amphiphilic nature and easily modifiable surface of the PAMAM dendrimer makes it an attractive vehicle for targeted drug delivery and molecular imaging. The use of these systems for therapeutic delivery applications has been limited by the quantity and chemical nature of the encapsulated agent. While the nanoscopic size and amphiphilicity of dendrimers are important features for drug delivery, it would be attractive to be able to manipulate this system to enhance encapsulation and release of different agents. Self-assembly of partially fluorinated PAMAM into larger particulates preserves dendrimer integrity and creates a dense incorporation of fluorines sufficient to enable noninvasive observation by $^{19}$F MRI. We therefore hypothesized that the self-assembly of

* Corresponding author. Malone Engineering Center, 55 Prospect Street, New Haven, CT 06511, USA. Tel.: +1 203 432 1043; fax: +1 203 432 0030.
*E-mail address:* tarek.fahmy@yale.edu (T.M. Fahmy).

0142-9612/$ – see front matter © 2009 Elsevier Ltd. All rights reserved.
doi:10.1016/j.biomaterials.2009.04.014

partially fluorinated PAMAM dendrimers into larger particulates may enhance the range of utility of these systems in drug delivery and molecular imaging applications.

## 2. Materials and methods

### 2.1. Fabrication of fluorinated dendrimer-based particulates

#### 2.1.1. Synthesis and $^{19}F$ NMR characterization of fluorinated PAMAM(G3) dendrimers

Ten milligrams of PAMAM Generation 3 (PAMAM(G3)) starburst dendrimers [Aldrich] were desiccated in a 24 mL glass scintillation vial. The dendrimer was then dissolved in anhydrous dimethyl sulfoxide (DMSO) [Alfa Aesar] at a 5 mg/mL final concentration. This solution was charged with 250 molar equivalents of triethylamine (TEA) [Sigma] and 25 molar equivalents of heptafluorobutyric acid anhydride (HFAA) [Pierce]. The reaction mixture was agitated vigorously for 2 h at 25 °C. An aliquot of the reaction mixture was prepared in chloroform-D [Cambridge Isotope Laboratories, Inc.] with a 0.1% v/v trifluoroethanol (TFE) [J.T. Baker] internal standard for characterization by $^{19}F$ NMR on a 400 MHz spectrometer [Bruker]. Extent of fluorination was quantified by comparison of the $CF_3$ relative integrated peak areas for the internal standard and the fluorinated PAMAM(G3) dendrimers (Supplementary Fig. 1). This synthetic approach was carried out for dendrimer solutions having final concentrations of 1, 2.5, 5, and 10 mg/mL. PAMAM(G3) dendrimers were also fluorinated with either pentafluoropropionic acid anhydride (PFAA) [Pierce] or trifluoroacetic acid anhydride (TFAA) [Pierce] and characterized by $^{19}F$ NMR. The fluorination of PAMAM(G3) dendrimers was performed across a stoichiometric range of HFAA and PFAA (Table 1) to vary the fluorine-to-amine ratio.

#### 2.1.2. Synthesis and $^{19}F$ NMR characterization of fluorinated PAMAM(G6) dendrimers

Generation 6 PAMAM starburst dendrimers [Aldrich] were fluorinated as described above by proportionally adjusting the initial molar equivalents of HFAA and TEA to account for the increase in surface amines compared with PAMAM(G3) dendrimers (Table 1). $^{19}F$ NMR characterization was performed as described above. This synthetic approach was carried out with dendrimer solutions having final concentrations of 5, 10 and 20 mg/mL. PAMAM(G6) dendrimers were also fluorinated across a stoichiometric range of HFAA (Table 1).

#### 2.1.3. Formation of fluorinated PAMAM dendrimer-based particulates

An equivolume of MilliQ purified, deionized water ($d_iH_2O$) was added to the fluorinated PAMAM dendrimer reaction mixture described above and mixed vigorously to yield a cloudy, white precipitous suspension. Subsequent heating in a 100 °C water bath for 1 h yielded an aggregated white precipitate that was adherent to the glass surface. The supernatant was decanted and the precipitate washed four times with two volumes of $d_iH_2O$. The precipitate was then lyophilized for 24 h in a FreezeZone 1 [Labconco] for further characterization.

### 2.2. Critical temperature ($T_c$) of fluorinated PAMAM(G3) dendrimer-based particulate formation

Fluorinated PAMAM(G3) dendrimer-based particulates were formulated as described above with the following exceptions: the initial dendrimer concentration was restricted to 10 mg/mL and the water bath was adjusted to defined temperatures across the range of 25–100 °C. The resulting white precipitate that was adherent to the glass surface was washed four times with two volumes of $d_iH_2O$ and lyophilized for 24 h for further characterization.

### 2.3. Perturbations to fluorinated PAMAM(G3) dendrimer-based particulate formation

Fluorinated PAMAM(G3) dendrimer-based particulates were formulated as described above with the following exception: the aqueous phase was modified according to Table 2 prior to delivery. Following heating at 100 °C, the white precipitate that was adherent to the glass surface was washed four times with two volumes of $d_iH_2O$ and lyophilized for 24 h for further characterization.

### 2.4. Scanning electron microscopy

Fluorinated PAMAM dendrimer-based particulate morphology was analyzed by scanning electron microscopy [XL-30 ESEM-FEG, FEI Company]. A monolayer of dry particulates was mounted on an aluminum stub using double-sided carbon tape and coated with a thin layer of gold using a sputter coater [Cressington]. The coated samples were imaged using an electron acceleration of 10 keV. Size distribution and average particulate diameter were determined by analyzing 160 particulates per image using the freeware program NIH ImageJ.

### 2.5. Transmission electron microscopy

The internal structure of fluorinated PAMAM(G3) particulates was probed by transmission electron microscopy (TEM). Particulates were either directly embedded in Embed-812 [Electron Microscopy Sciences] or treated with 1.0% $OsO_4$ in 0.1 M HEPES buffer, pH 7.4 for 30 min at 25 °C, prior to standard resin embedding. After polymerization ultrathin (~80 nm) sections were prepared on a Reichert-Jung Ultracut E microtome, mounted on Formvar film-coated 200 mesh nickel grids [Electron Microscopy Sciences] and imaged unstained or stained with uranyl acetate and lead citrate according to standard protocols. High-resolution digital electron

**Table 2**
Characteristics of the colloidal system.

| PAMAM (mg/mL) | HFAA:PAMAM | TEA:HFAA | Aqueous phase | Salt (mM) | pH |
|---|---|---|---|---|---|
| 10 | 25:1 | 10:1 | – | 0 | 2–10 |
| 5 | 25:1 | 10:1 | – | 0 | 2–10 |
| 2.5 | 25:1 | 10:1 | – | 0 | 2–10 |
| 1 | 25:1 | 10:1 | – | 0 | 2–10 |
| 10 | 25:1 | 10:1 | $H_2PO_4^-$/ $HPO_4^{2-}$ | 100 | 2, 7, 12 |
| 5 | 25:1 | 10:1 | $H_2PO_4^-$/ $HPO_4^{2-}$ | 100 | 2, 7, 12 |
| 2.5 | 25:1 | 10:1 | $H_2PO_4^-$/ $HPO_4^{2-}$ | 100 | 2, 7, 12 |
| 1 | 25:1 | 10:1 | $H_2PO_4^-$/ $HPO_4^{2-}$ | 100 | 2, 7, 12 |
| 10 | 25:1 | 10:1 | NaCl | 100, 500 | – |
| 5 | 25:1 | 10:1 | NaCl | 100, 500 | – |
| 2.5 | 25:1 | 10:1 | NaCl | 100, 500 | – |
| 1 | 25:1 | 10:1 | NaCl | 100, 500 | – |
| 10 | 25:1 | 10:1 | $NaNO_3$ | 100, 500 | – |
| 5 | 25:1 | 10:1 | $NaNO_3$ | 100, 500 | – |
| 2.5 | 25:1 | 10:1 | $NaNO_3$ | 100, 500 | – |
| 1 | 25:1 | 10:1 | $NaNO_3$ | 100, 500 | – |
| 10 | 25:1 | 10:1 | $Na_2SO_4$ | 100, 500 | – |
| 5 | 25:1 | 10:1 | $Na_2SO_4$ | 100, 500 | – |
| 2.5 | 25:1 | 10:1 | $Na_2SO_4$ | 100, 500 | – |
| 1 | 25:1 | 10:1 | $Na_2SO_4$ | 100, 500 | – |

**Table 1**
Comparison of fluorinated PAMAM dendrimer-based formulations.

| Generation | PAMAM (mg/mL) | HFAA: PAMAM | PFAA: PAMAM | TFAA: PAMAM | # Fluorines | # $NH_2$ | Morphology |
|---|---|---|---|---|---|---|---|
| 6 | 20 | 200:1 | – | – | – | – | Spherical |
| 6 | 10 | 200:1 | – | – | – | – | Spherical |
| 6 | 5 | 200:1 | – | – | 266 | 218 | Spherical |
| 6 | 10 | 100:1 | – | – | – | – | Fused, disordered |
| 3 | 10 | 25:1 | – | – | – | – | Spherical |
| 3 | 5 | 25:1 | – | – | 105 | 17 | Spherical |
| 3 | 2.5 | 25:1 | – | – | – | – | Spherical |
| 3 | 1 | 25:1 | – | – | – | – | Fused, disordered |
| 3 | 10 | 12.5:1 | – | – | – | –– | Spherical |
| 3 | 10 | 50:1 | – | – | – | – | Spherical |
| 3 | 5 | – | 18:1 | – | 75 | 17 | Disordered |
| 3 | 5 | – | 25:1 | – | 105 | 11 | Fused, disordered |
| 3 | 5 | – | 35:1 | – | 115 | 9 | Spherical |
| 3 | 5 | – | – | 25:1 | – | – | None |
| 3 | 5 | – | – | 50:1 | – | – | None |
| 3 | 5 | – | – | 100:1 | – | – | None |

micrographs were acquired on a Philips Tecnai Biotwin – T12 electron microscope using Morada Soft Imaging System CCD (3700 × 2500 pixels).

The internal structure of fluorinated PAMAM(G3) particulates was also examined by TEM following generation of suitable freeze fracture replicas. Particulates were immersed in 0.1 M HEPES buffer, pH 7.4 and cryoprotected with 25% glycerol in 0.1 M HEPES prior to rapid freezing in liquid ethane. Replicas were prepared on a Balzers Freeze-Etch apparatus (BAF 400D) using gold specimen supports for double replication. Specimens were cleaved at −110 °C under appropriate, high vacuum conditions (<$5 \times 10^{-6}$ mbar). Replication was achieved by shadowing with 2 nm platinum at an angle of 45° followed by 20 nm of carbon at 90°. Replicas were incubated overnight in 50% chromosulfuric acid, rinsed 6 times in HPLC purified distilled water and mounted on Formvar coated nickel grids. High-resolution digital micrographs of the freeze fracture replicas were acquired as described above.

### 2.6. pH-dependent disassembly of fluorinated PAMAM dendrimer-based particulates

Disassembly of fluorinated PAMAM(G3) dendrimer-based particulates was monitored by absorbance at 225 nm on a SpectraMax M5 cuvette reader [Molecular Devices] equipped with SoftMax Pro 4.8 processing software. One and one half milligrams of fluorinated PAMAM(G3) particulates were delivered to a quartz cuvette charged with 1 mL of either 20 mM citrate buffer at pH 7 or pH 5. Suspensions were mixed manually prior to each scan for a 30-minute duration. At $t = 30$ min, 25 μL of 1 N HCl were delivered to the pH 7 suspension to initiate and terminate denaturation. Reference spectra were collected for each respective buffer to establish an appropriate baseline. The raw data for pH 5 was fit with the "sigmoidal dose-response (variable slope)" function given by:

$$Y_0 + \frac{(Y_{max} - Y_0)}{1 + 10^{[(\log[EC_{50}] - x) - H]}} \quad (1)$$

where $EC_{50}$ is the midpoint between $Y_0$ and $Y_{max}$ and $H$ is the Hill coefficient. Similar measurements at pH 7, 6, 5 and 2 were also performed with fluorinated PAMAM(G3) dendrimer-based particulates by monitoring absorbance at 600 nm. Dispersion represents an increase in optical density ($OD_{600}$), where disassembly and solubilization represent a decrease in $OD_{600}$. The raw data for pH 7 was fit with the "one phase exponential association" function given by:

$$Y_{max_1}\left(1 - \exp^{-k_1 x}\right) \quad (2)$$

with the constraint that $K_1 > 0$, and the raw data for pH 6, 5, and 2 was fit with the "one phase exponential decay" function given by:

$$Y_{max_1}\left(\exp^{-k_1 x}\right) \quad (3)$$

with the constraint that $K_1 > 0$. All of the raw data fits were performed with the Prism V4.0b software suite [GraphPad].

### 2.7. Zeta potential measurements

Two milligrams of fluorinated PAMAM(G3) dendrimer-based particulates were dissolved into 2 mL of 20 mM citrate buffer prepared at either pH 7.0, 5.0, or 2.0, thoroughly mixed, and allowed to equilibrate. Zeta potential measurements were obtained with a ZetaPALS instrument [Brookhaven Instruments Corporation]. Equilibrium measurements were collected manually by averaging ten runs comprised of twenty cycles per run.

### 2.8. Encapsulation of small molecules by fluorinated PAMAM(G3) dendrimer-based particulates

Twenty-five milligrams of PAMAM(G3) starburst dendrimers were dried in a 24 mL glass scintillation vial. The dendrimer was then dissolved into anhydrous DMSO to a 5 mg/mL final concentration. This solution was charged with 250 molar equivalents of TEA and 25 molar equivalents of HFAA. The reaction mixture was agitated vigorously on an orbit shaker for 2 h at 25 °C. An equivolume aliquot of 0.4 mg/mL Rhodamine B [Acros Organics] in $d_iH_2O$ was added to the fluorinated PAMAM(G3) dendrimer reaction mixture and mixed vigorously to yield a cloudy, pink precipitous suspension. Subsequent heating in a 100 °C water bath for ~1 h yielded an aggregated pink precipitate that was adherent to the glass surface. The supernatant was decanted and the precipitate washed eight times with two volumes of $d_iH_2O$ to remove excess Rhodamine B. The precipitate was lyophilized for 24 h.

### 2.9. Controlled release kinetic analysis

Each of three 1 kDa molecular weight cut off dialysis columns [Amersham Biosciences] were charged with 2.75 mg of Rhodamine B encapsulated fluorinated PAMAM(G3) particulates and 500 μL of 20 mM citrate buffer prepared at either pH 7.0, 5.0, or 2.0. Each column was dialyzed against 15 mL of 20 mM citrate buffer with corresponding pH with stirring at 25 °C in the dark for 48 h. 100 μL aliquots were removed from the 15 mL dialysis buffer reservoir in time and transferred to a Microtest black/clear bottom 96-well assay plate [BD Biosciences]. Immediate endpoint fluorescence intensity measurements (Ex. 540 nm/Em 625 nm) were performed on a SpectraMax M5 plate reader [Molecular Devices] equipped with SoftMax Pro 4.8 processing software. The raw data was fit with the "two phase exponential association" function given by:

$$Y_{max_1}\left(1 - \exp^{-k_1 x}\right) + Y_{max_2}\left(1 - \exp^{-k_2 x}\right) \quad (4)$$

with the constraints that $Y_{max_2}$ and $K_1$ and $K_2 > 0$.

### 2.10. Analysis of cytotoxicity

Fluorinated PAMAM(G3) particulates, PAMAM(G3), PAMAM(G4), and PAMAM(G6) were suspended in 1× PBS at a final concentration of 2 mg/mL and subsequently UV-sterilized for 10 min. 200 μL aliquots of each were plated separately in triplicate on 96-well plates and serially diluted by 100 μL aliquots of complete medium. Sterile 1× PBS and 10% w/v $NaN_3$ were plated in duplicate and serially diluted, as described above, to establish a positive and negative control, respectively. Chinese hamster ovarian (CHO) cells were adjusted to $1 \times 10^6$ cells/mL in complete medium. Per well, $1 \times 10^5$ CHO cells were plated and incubated at 37 °C for 4 h. Cell viability was analyzed via the Cell Titer Blue fluorescence assay according to the manufacturer's protocol [Promega].

### 2.11. T1 relaxation kinetics

Suspensions of fluorinated PAMAM(G3) particulates at 5 mg/mL were prepared in each of three 20 mM sodium citrate buffers prepared at pH 7.0, 5.0, and 2.0, respectively. Suspensions were sonicated in a Model 50D water bath sonicator [VWR] to disperse the particulates and placed on a rototorque [LabQuake] for 18 h to engage disassembly. Individual phantoms were prepared in 5-mL polypropylene tubes by addition of 20% w/v gelatin and placed into a volume radio-frequency (RF) coil with an inner diameter of 1 cm and a length of 1.5 cm. $T1$ relaxation times were obtained using the method of progressive saturation. Signal amplitudes were fit to

$$S = S_{max}(1 - \exp[-(T_R/T1)]) \quad (5)$$

where $T_R$ is variable repetition time.

### 2.12. Gelatin phantom $^{19}F$ chemical shift imaging

A 250 μL aliquot of 10% w/v gelatin solution prepared in 1× PBS was delivered to a 5 mL polypropylene tube to establish a blank gelatin phase. A 20 mg/mL suspension of fluorinated PAMAM(G3) particulates was prepared in 1× PBS. A 250 μL aliquot of the suspension was charged with 250 μL of 20% w/v gelatin solution and delivered to the 5 mL polypropylene tube to establish a sample-containing gelatin phase; however, upon solidification, the particulates were observed to aggregate and settle in the center of the meniscus of the blank gelatin phase. The layered system was capped with a blank gelatin phase by the addition of a 250 μL aliquot of 10% w/v gelatin solution. Imaging was performed with a cylindrical volume (1 cm diameter × 1.5 cm) RF coil that could be tuned to either 170.5 MHz for $^1H$ or 160.5 MHz for $^{19}F$. The layered phantom was positioned in a 4.0 T 80-mm horizontal bore imaging system (Bruker). A $^1H$ image was acquired using a 2DFT spin-echo sequence with TR/TE = 500/10 ms and 128 × 128 image points. An $^{19}F$ image was acquired by chemical shift imaging (CSI) sequence, centered on the $CF_3$ resonance, with TR = 500 and 128 × 32 × 32 image points. Two millimeter-thick coronal slices were acquired for both $^1H$ and $^{19}F$ with exactly the same coordinates. The number of averages was 1 and 8 for the $^1H$ and $^{19}F$ images, respectively, and the total imaging time was 4 h.

### 2.13. Magnetic resonance $^{19}F$ chemical shift imaging

Experiments were performed in accordance with the regulations set by the Yale Animal Resource Center (YARC). MRI experiments were carried out on a female B6 mouse, 7–8 weeks of age, which was maintained in the animal facilities of the Malone Engineering Center at Yale University. The mouse was anaesthetized by an intraperitoneal (i.p.) injection of ketamine in PBS, intubated, and connected to a mechanical ventilator delivering a mixture of $O_2/N_2$/isofluorane to maintain anesthetic effects and viability. The inferior vena cava (IVC) of one mouse was surgically catheterized before the liver with a 10 μm-diameter polypropylene tube connected to a syringe. The mouse was positioned in a 4.0 T 80-mm horizontal bore imaging system [Bruker] and the torso anatomy was imaged immediately using a single turn 3 cm × 3 cm surface RF coil that could be tuned to either 170.5 MHz for $^1H$ or 160.5 MHz for $^{19}F$. The anatomical images of the torso were acquired with 4 transverse slices through the liver and kidney regions using a respiratory-gated gradient echo sequence with TR/TE = 400/4.9 ms and 256 × 256 imaging points. Using the setup described above, 200 μL of a 20 mg/mL solution of PEGylated fluorinated PAMAM(G3) particulates in 100 mM borate buffer pH 9.0 was slowly injected intravenously (i.v.) and imaged immediately. $^{19}F$ CSI images were acquired with selection for the $CF_3$ resonance, with TR = 400 ms and 256 × 64 × 64 image points. Two millimeter-thick slices were acquired for both $^1H$ and $^{19}F$ with exactly the same coordinates. The number of averages was 1 and 8 for the $^1H$ and $^{19}F$ images, respectively, and the total imaging time was 4 h.

### 2.14. $^{19}F$ chemical shift image processing

$^{19}F$ CSI data and associated $^{1}H$ anatomical data were transferred to a workstation and reconstructed by a simple fast Fourier transform technique using BioImage Suite software. The $CF_3$ resonance was identified manually and the spectrum around the peak was integrated to construct the fluorine image. Fluorine images were then overlaid onto corresponding anatomical maps.

## 3. Results and discussion

### 3.1. Synthesis and characterization of fluorinated PAMAM dendrimer-based particulates

PAMAM(G3) dendrimers were covalently modified with 15 heptafluoroacyl groups by reaction of the amine surface with heptafluorobutyric acid anhydride (HFAA) in the presence of triethylamine (TEA). These products were subsequently extracted into water to initiate the fluorophobic effect (Fig. 1). With sufficient thermal energy, we observed spontaneous aggregation of the fluorinated PAMAM dendrimers. Scanning electron microscopy revealed the formation of spherical particulates (Fig. 1f). Given that fluorophobic interactions provided the cohesive forces driving aggregation, a densely packed sphere was expected. Transmission electron microscopy (TEM) of the particulates confirmed this densely packed configuration (Fig. 1g). Further, TEM of a freeze fracture replica of the particulates revealed a matrix-like internal structure composed of nanoscale subunits of 10–20 nm, which we hypothesize to be the partially fluorinated dendrimer subunits (Fig. 1h).

### 3.2. Control of the self-assembly of fluorinated PAMAM dendrimer-based particulates

To investigate the optimal set of fluorination conditions necessary for the formation of stable particulates, we chose to examine the effects of manipulating the fluorine-to-amine ratio of the fluorinated dendrimer. First, we varied the perfluoroalkyl chain length of the acylating agent used to modify PAMAM(G3) dendrimers (Table 1). We found that dendrimers modified with PFAA required a two-fold higher fluorine-to-amine ratio to enable the formation of stable particulates when compared to those modified with HFAA, while those modified with TFAA failed to yield visible precipitous aggregation. Next, we varied the extent of the fluorination by controlling the stoichiometric ratio of HFAA to PAMAM(G3) or PAMAM(G6) dendrimer (Table 1) and observed that insufficient fluorination led to the formation of disordered architectures. Finally, it was observed that particulates could be formed with both PAMAM(G3) and PAMAM(G6) dendrimers modified with

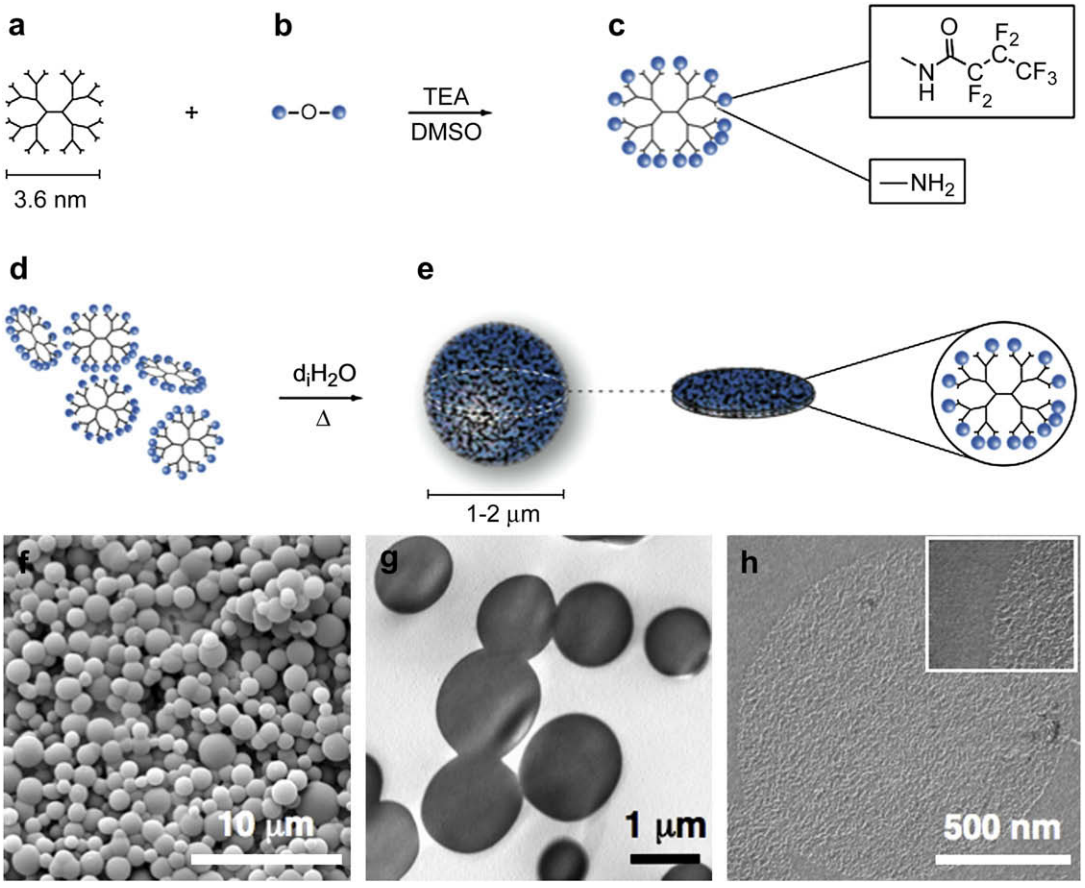


**Fig. 1.** Self-assembly model of fluorinated, PAMAM(G3) dendrimer-based particulates. Fifteen primary amines on the surface of (a) PAMAM(G3) starburst dendrimers were functionalized through reaction with (b) HFAA to yield (c) heptafluoroacylated PAMAM(G3) terminal branches. The blue sphere and the branch terminus represent the heptafluoroacyl substituent and the terminal primary amine, respectively. The (d) randomized mixture of partially fluorinated dendrimers aggregated in aqueous environment and formed (e) self-assembled particulates with the addition of sufficient thermal energy (100°C for 1 h). The cross-sectional diameter of the particulate in (e) illustrates the densely packed internal network of partially fluorinated dendrimers. (f) Scanning electron micrograph of the fluorinated PAMAM(G3) dendrimer-based particulates formulated with 5 mg/mL initial concentration of PAMAM(G3) dendrimers and 25 molar equivalents of HFAA. Scale bar is 10 μm. (g) Transmission electron micrograph of 80-nm-thick cross-section of the particulates in (f) treated with 1.0% $OsO_4$, embedded in Embed-812 epoxy, and stained with uranyl acetate and lead citrate. Scale bar is 1 μm. (h) Transmission electron micrograph of a freeze fracture replica of the particulates in (f) depicting a dense matrix-like internal structure upon cross-fracture. Scale bar is 500 nm.

15 and 38 heptafluoroacyl substituents, respectively. This suggests that a geometrical constraint with respect to the presentation of the perfluoroalkyl substituents on the dendrimer surface might play a role in particulate formation. These observations strongly suggest that fluorophobic interactions drive the particulate self-assembly. We also note that an optimal set of fluorination conditions necessary for the formation of stable particulates exists. These qualitative results establish that the driving force responsible for the self-assembly of the particulates is the fluorophobic effect.

Thermal energy also plays a critical role in self-assembled systems driven by non-covalent interactions because of the necessity to surmount entropic costs. By independently varying the temperature, we determined that a critical temperature ($T_c$) of 50 °C existed (Fig. 2a). At temperatures below this critical point, initial aggregation resulted in disordered precipitation, rather than particulate formation. In conjunction with the results above, we demonstrate that thermodynamic control governs the formation of these particulates.

The nucleation and aggregation responsible for particulate formation is driven by a critical coagulation concentration (C.C.C.) described by the equation:

$$\text{c.c.c.} = \frac{(4\pi\varepsilon_o)^3 0.107\varepsilon_r^3 (kT)^5 Z^4}{N_A A^2 (ze)^6} \quad (6)$$

where $k$ is Boltzman's constant, $T$ is temperature, $Z$ is zeta potential, $z$ is charge, $\varepsilon_o$ is the permittivity of free space, $\varepsilon_r$ is , $N_A$ is Avagadro's number, and $A$ is an arbitrary constant [26]. To examine the colloidal properties of this assembly, we chose to manipulate specific parameters of this equation. Since partial fluorination renders unreacted primary amines susceptible to protonation, we chose to adjust the pH of the reaction mixture to control the zeta potential (Table 2). In buffered and unbuffered conditions, we noticed a trend consistent with Equation (6). In unbuffered conditions particulate formation was observed at pH ≥10.0 (Fig. 2b), thus the higher zeta potential created at lower pH resulted in an increase to the C.C.C. For phosphate buffered conditions the zeta potential at pH ≥7.0 enabled particulate formation (Fig. 2c). The slight discrepancy in the critical point for pH was largely due to the presence of the buffering salts. Consistent across both sets of conditions, particulate formation at the zeta potential created at low pH would require elevated initial dendrimer concentrations to compensate for increases in the C.C.C. To determine the effects of charge on particulate formation, we utilized the aqueous addition of salts comprising -1 and -2 charged counterions to facilitate control over the reaction mixture charge (Table 2). Here, we also noted a trend consistent with Equation (6). Increasing the anionic charge of the salt counterion enabled particulate formation at lower initial dendrimer concentrations (Fig. 2d).

### 3.3. Control over the size of fluorinated PAMAM(G3) dendrimer-based particulates

One of the advantages of this assembly process is that modulation of the initial dendrimer concentration can easily control the particulate

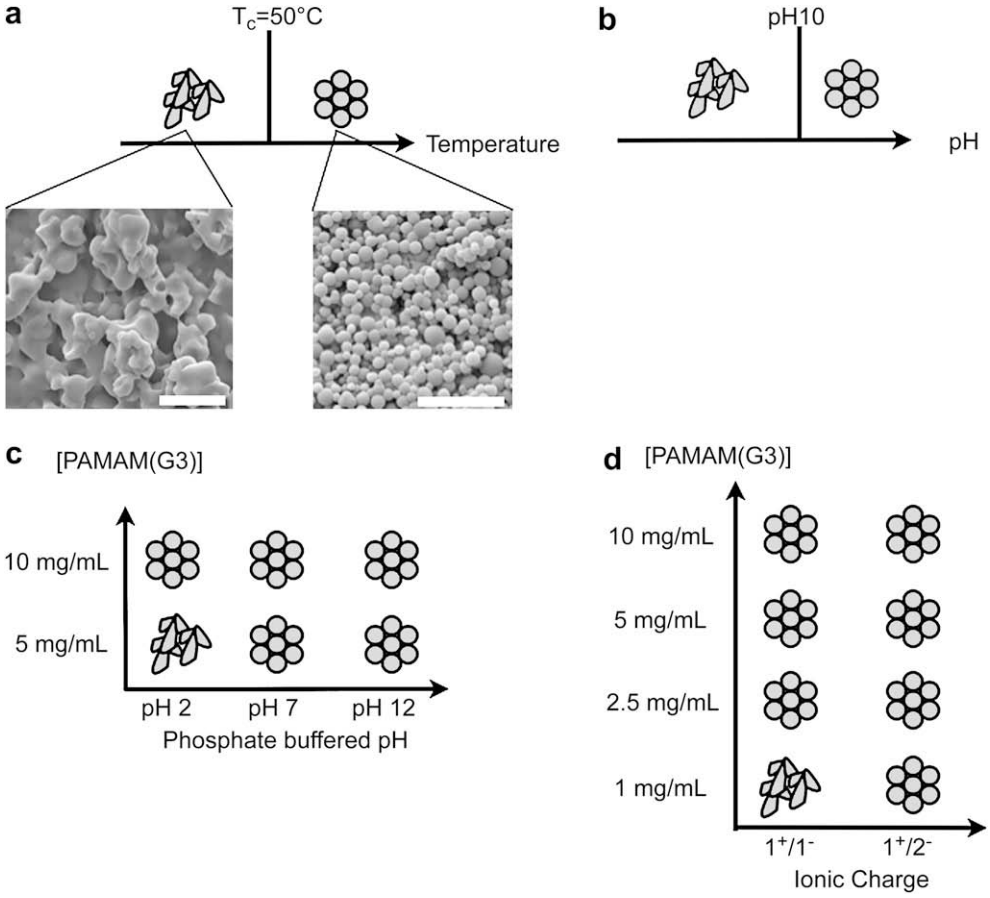


**Fig. 2.** Colloidal properties of fluorinated, PAMAM(G3) dendrimer-based particulates. (a) The critical temperature ($T_c$) required for formation of stable particulates was determined to be 50 °C. The gray spheres and disordered fragments are representations of the inset SEM images of the particulates and disordered architectures, respectively. Scale bars are 10 μm. Effects of (b) unbuffered and (c) phosphate buffered pH environments on the C.C.C. and particulate formation. (d) Effects of counterion charge on the C.C.C. and particulate formation.

diameter. We demonstrated this by varying the concentration of PAMAM(G3) dendrimer fluorinated with 25 molar equivalents of HFAA (Fig. 3). An initial concentration of 10 mg/mL of fluorinated PAMAM(G3) dendrimer provided adequate nucleation and aggregation for the formation of large (~3 μm) polydisperse particulates (Fig. 3a). Decreasing the initial dendrimer concentration toward the C.C.C. both decreased the particulate size and dramatically narrowed the polydispersity (Fig. 3b and c). Aggregation at 1 mg/mL generated fused and disordered architectures and no formation of particulates was observed in the absence of the dendrimer. Increasing the dendrimer generation while maintaining the same extent of fluorination has negligible effects on particulate size distribution (data not shown).

### 3.4. Fluorinated PAMAM(G3) dendrimer-based particulates are pH-responsive

Since these dense particulates are formed by aggregation of the heptafluoroacyl substituents due to the fluorophobic effect, we reasoned that these assemblies might exhibit sensitivity to the pH of the external environment. This is because partial fluorination of the dendrimer subunits results in interspersed amines that may be protonated at low pH, inducing electrostatic interactions that could surmount the fluorophobic-driven stability of the particulate and elicit disassembly via a repulsion event.

To investigate the effect of pH on these particulates, we inferred that the disassembly could be monitored intrinsically by following the absorption wavelength of the characteristic $n \rightarrow \pi^*$ transition of the amide bond ($\lambda_{max} = 225$ nm). This is because the disassembly event would effectively expose the hidden amide bonds either inherent to the dendrimer core or resultant of the reaction of the perfluorocarboxylic acid anhydride with PAMAM(G3) amine surface (Fig. 1). Similarly, we deduced that the disassembly could also be monitored globally by following changes in bulk solution dispersivity at an optical density of 600 nm ($OD_{600}$). This is because dispersion of intact particulates would result in an increase in $OD_{600}$, whereas their disassembly and subsequent solubilization would cause a decrease in $OD_{600}$. By these methods, we observed that fluorinated PAMAM(G3) particulates were indeed sensitive to pH changes of the external environment, as their disassembly was strongly dependent on pH (Fig. 4a–c). This disassembly event was determined to be irreversible.

Further, to establish that the electrostatic repulsive forces were indeed responsible for driving particulate disassembly, we examined the zeta potential of particulates following exposure to different external pH environments. We observed a positive increase in zeta potential with decrease in external pH (Fig. 4d), demonstrating that electrostatic repulsion disrupts particulate stability.

### 3.5. pH-induced controlled release of small molecules

The inherent pH-responsive capabilities of these particulates in the range of 7–5, in concert with their size, have attractive

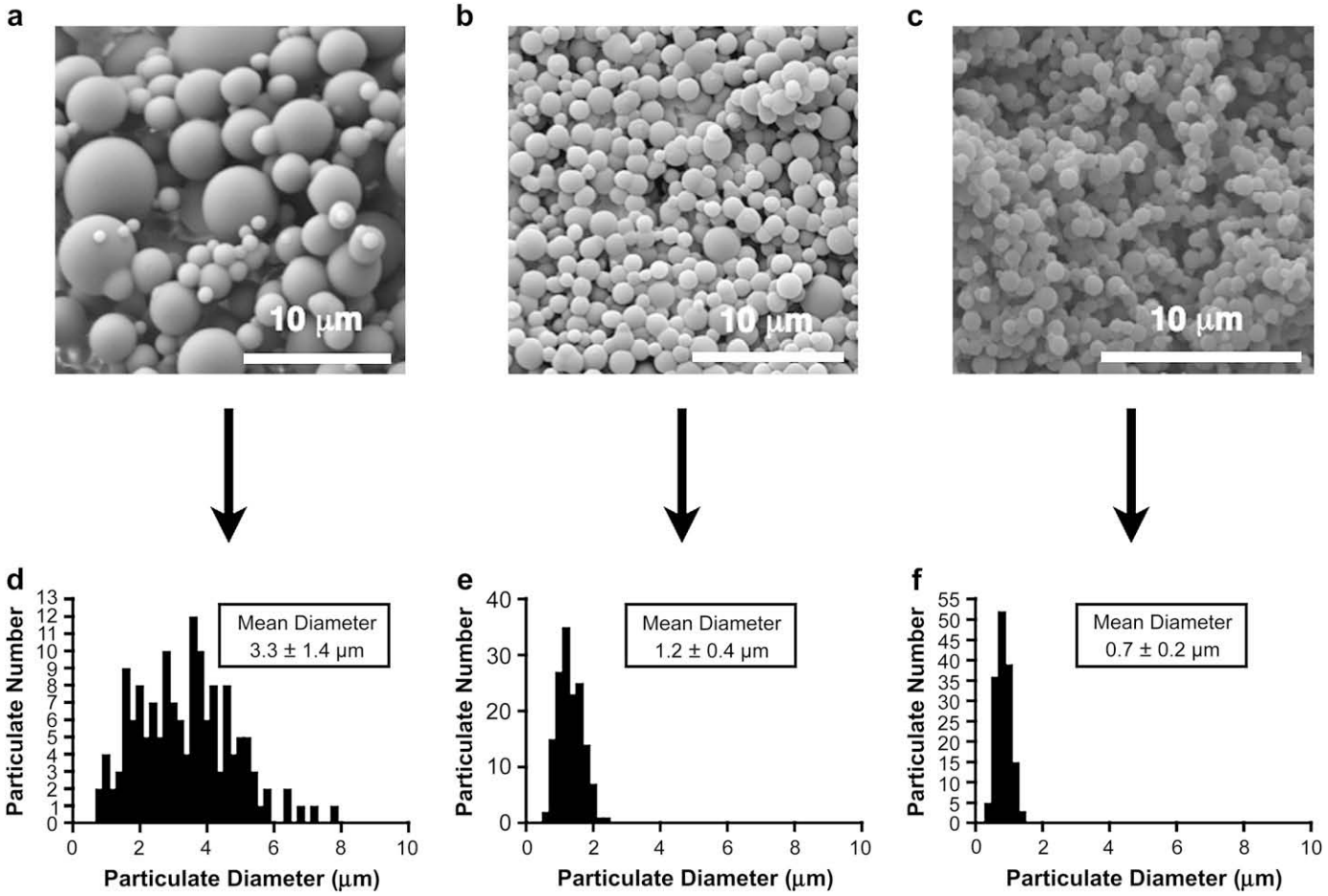


**Fig. 3.** Dependence of particulate size on initial fluorinated PAMAM(G3) dendrimer concentration. PAMAM(G3) dendrimers at initial concentrations of 10, 5, 2.5 and 1 mg/mL were fluorinated with 25 molar equivalents of HFAA. Particulates were formed from fluorinated PAMAM(G3) dendrimers at (a) 10 mg/mL, (b) 5 mg/mL, and (c) 2.5 mg/mL by heating at 100°C for 1 h. Particulate size distributions were determined for (d) 10 mg/mL, (e) 5 mg/mL, and (f) 2.5 mg/mL formulations using NIH ImageJ software. The mean particle diameters calculated were 3.3 ± 1.4 μm, 1.2 ± 0.4 μm, and 0.7 ± 0.2 μm for (a)–(c), respectively. Scale bars are 10 μm.

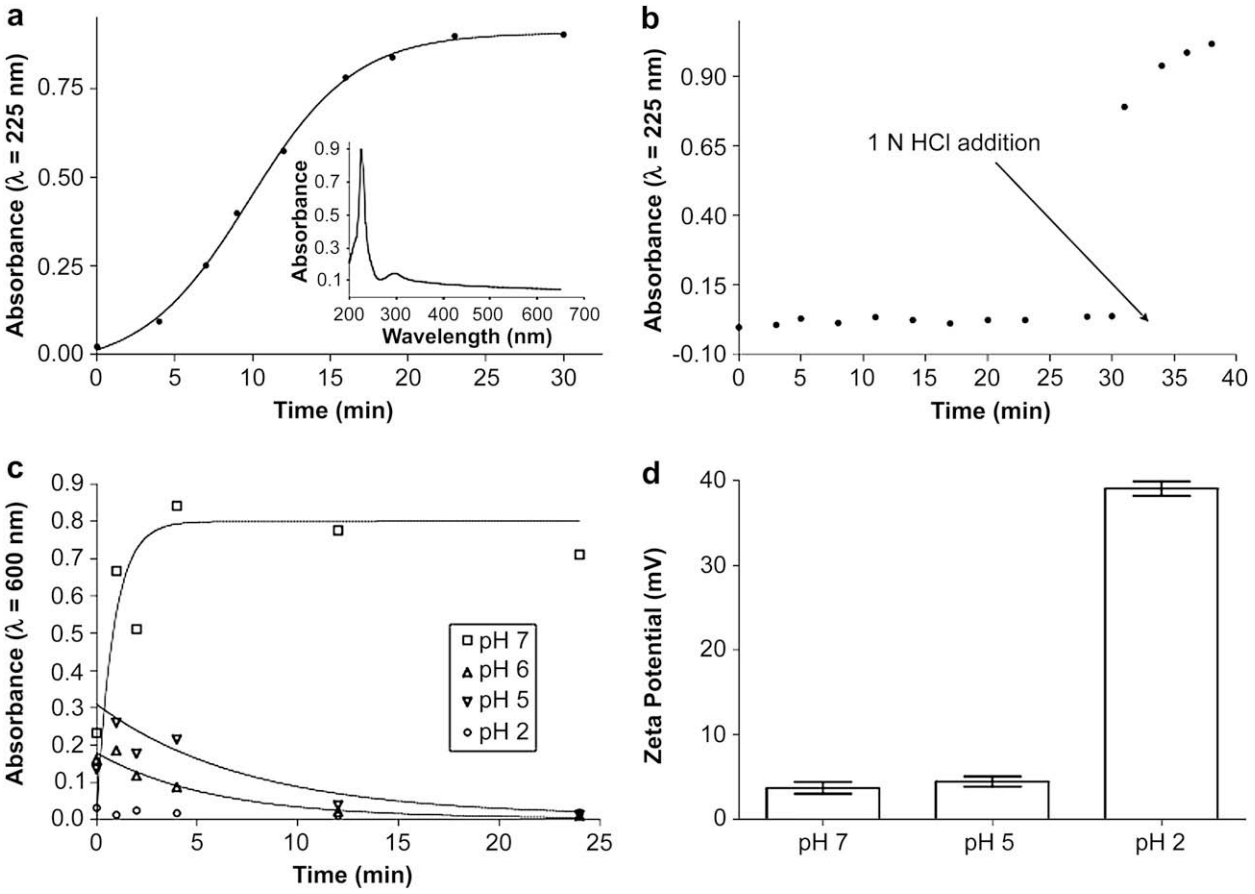


**Fig. 4.** Effects of external pH on fluorinated, PAMAM(G3) dendrimer-based particulates. (a) Spectrophotometric determination ($\lambda_{max} = 225$ nm) of the intrinsic disassembly of fluorinated PAMAM(G3) dendrimer-based particulates at pH 5. (b) The particulates were stable at pH 7 and only disassemble upon sensing a low pH environment indicated by the addition of 1 N HCl. (c) Spectrophotometric determination (OD = 600 nm) of the global disassembly of fluorinated PAMAM(G3) dendrimer-based particulates at pH 7, 6, 5 and 2. Particulate disassembly was observed to be irreversible. (d) Equilibrium zeta potential measurements of fluorinated PAMAM(G3) dendrimer-based particulates following exposure to pH 7, 5, and 2 external environments.

applications for drug delivery. To investigate these applications, we encapsulated the fluorescent dye Rhodamine B as a model small molecule drug. We observed that the pH-induced disassembly resulted in controlled release of the encapsulated dye, with faster release kinetics in lower pH environments (Fig. 5). At pH 2, the release kinetics were approximately 2-fold faster than at pH 5 and 4-fold faster than at pH 7. These data demonstrate that fluorophobic effect-driven dendrimer self-assembly produces pH-responsive particulates, an important feature for drug delivery.

### 3.6. $^{19}F$ magnetic resonance imaging in vivo

$^{19}F$ MRI is a powerful noninvasive imaging modality because of negligible fluorine background from surrounding tissue. A critical limitation of this technique has been the ability to generate agents that comprise short $T1$ relaxation times for fast acquisition and offer sufficient signal-to-noise for detection. To date, these criteria have been met by either liposomes encapsulating perfluorocarbons [27] or liquid perfluorocarbon nanoparticles [28–34]. For example, cells loaded with perfluorocarbon nanoparticles comprising $>10^{12}$ fluorine spins per cell were sufficient for detection [28]. Since the self-assembly we observed was mediated by covalent attachment of perfluoroalkyl substituents to the surface of PAMAM dendrimers, we exploited this high fluorine spin density to noninvasively image the site-specific accumulation of the particulates with $^{19}F$ MRI. In this work, we performed the MR experiments with chemical shift imaging (CSI) [27,35] centered on the $CF_3$ resonance. Since $^{19}F$ CSI reports only on the detection of the fluorinated particulates, collection of a spatially and geometrically identical proton ($^1H$) image is necessary to obtain an appropriate anatomical map for

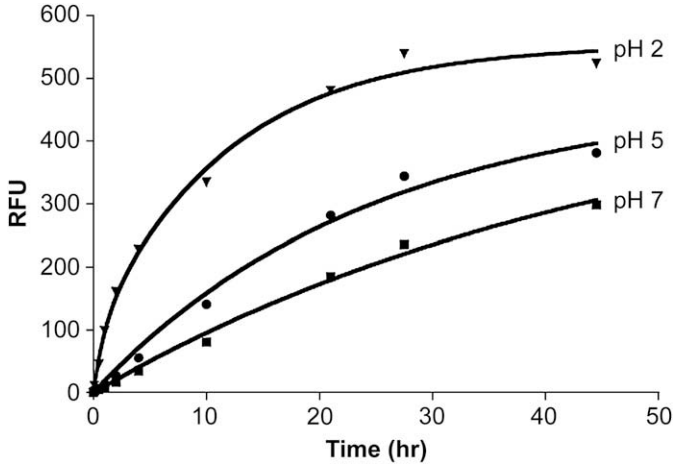


**Fig. 5.** Stimulus-induced controlled release of small molecules. Controlled release profiles for pH-dependent release of Rhodamine B over 48 h. Half-life$_1$ values obtained from the two phase exponential association fits of 33.32 h, 17.05 h, and 8.131 h for pH 7, pH 5, and pH 2, respectively, were observed to follow the trend consistent with the pH-dependent disassembly. -▼- represents pH 2, -●- represents pH 5, and -■- represents pH 7.

fluorine localization. To establish the sensitivity of this technique, a gelatin-based phantom containing a localized compartment of 5 mg of fluorinated PAMAM(G3) particulates was used for imaging with $^{19}$F CSI. The overlay of the $^{19}$F CSI image and its corresponding $^{1}$H image (Fig. 6a–c) demonstrates the capability of observing site-specific accumulation of fluorinated PAMAM(G3) particulates.

After demonstrating that the particulates possess a comparable biocompatibility profile to PAMAM Generation 6 dendrimers (Fig. 6d), we monitored their accumulation *in vivo* following *i.v.* injection into the mouse systemic circulation by $^{19}$F CSI. Prior to injection, the particulates were surface-modified with poly(ethylene glycol) (PEG) to enhance their circulation and transport properties in blood [36]. Particulates remain in the systemic circulation and are efficiently filtered by the liver (Fig. 7).

### *3.7. pH-induced changes in the magnetic resonance relaxivity of fluorinated PAMAM(G3) dendrimer-based particulates*

Particulate stability as a function of external microenvironment pH was assessed by probing the inherent lineshape characteristics and *T*1 relaxivity of the fluorinated PAMAM(G3) particulates' $CF_3$ resonance following dispersion into different physiologically relevant pH compartments: pH 7.4, 5.0, and 2.0. We observed a narrowing of the full-width at half-maximum from ~300 Hz to ~100 Hz that correlated with altering the pH environment from physiological pH to low pH (data not shown). Further, we observed strong pH-dependence in the *T*1 relaxation rates, as the inherent *T*1 relaxation time significantly increased with decreasing pH (Fig. 8a), indicating that the particulates maintain a stable and rigid structure of densely packed heptafluoroacyl substituents at physiological pH (Fig. 1) that

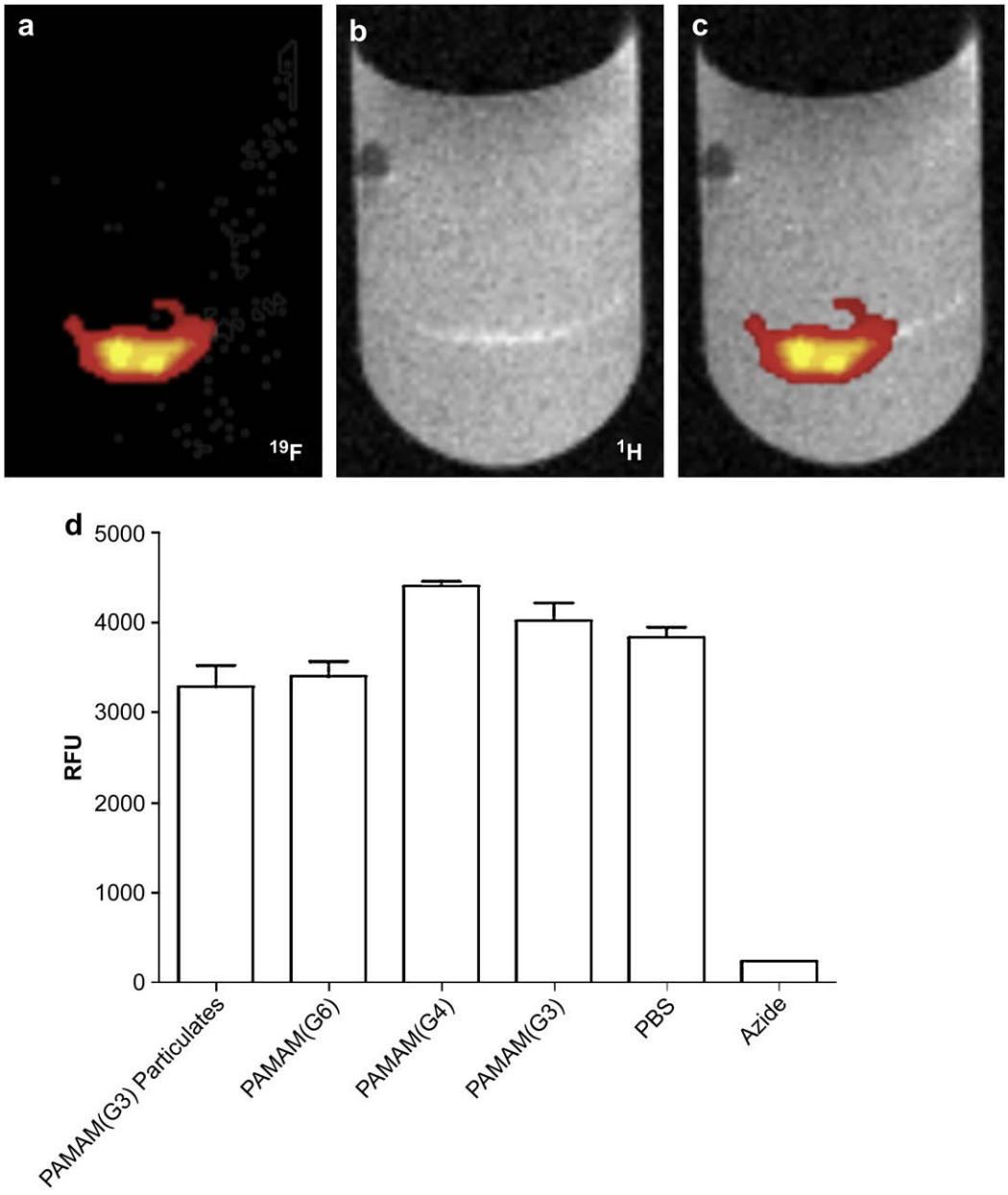


**Fig. 6.** Imaging with $^{19}$F MRI and biocompatibility. The overlay of the (a) $^{19}$F CSI image and (b) $^{1}$H image of the layered gelatin phantom illustrating the sensitivity for detection of fluorinated PAMAM(G3) particulates is presented in (c). Images were reconstructed by a fast Fourier transform technique using BioImage Suite [37]. The cytotoxic effects of 30 μg/mL fluorinated PAMAM(G3) particulates were compared to the effects of 30 μg/mL of PAMAM generations 3, 4, and 6 on Chinese hamster ovarian (CHO) cells (d).

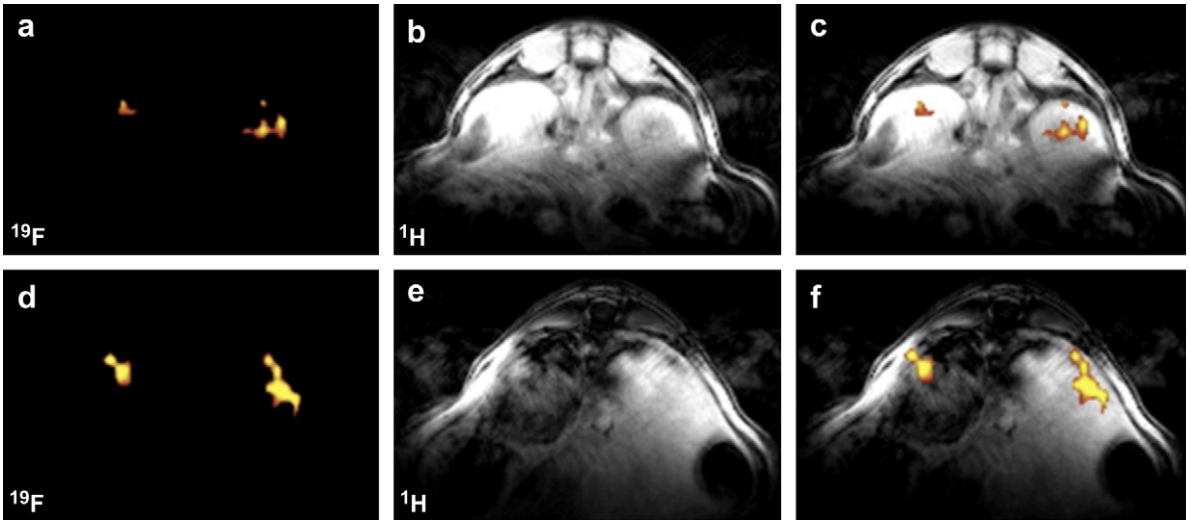


**Fig. 7.** Noninvasive imaging with $^{19}F$ MRI. The inferior vena cava (IVC) of female B6 mouse was surgically catheterized just below the level of the liver to enable intravenous (i.v.) injection of 4 mg of PEGylated, fluorinated PAMAM(G3) particulates. The overlay of the (a) $^{19}F$ CSI image and (b) $^{1}H$ image illustrating the presence of the PEGylated particulates in the mouse kidney vasculature after i.v. injection into the IVC is presented in (c). The overlay of the (d) $^{19}F$ CSI image and (e) $^{1}H$ image illustrating the filtration of the PEGylated particulates in the mouse liver after i.v. injection into the IVC is presented in (f). Images were reconstructed by a fast Fourier transform technique using BioImage Suite [37].

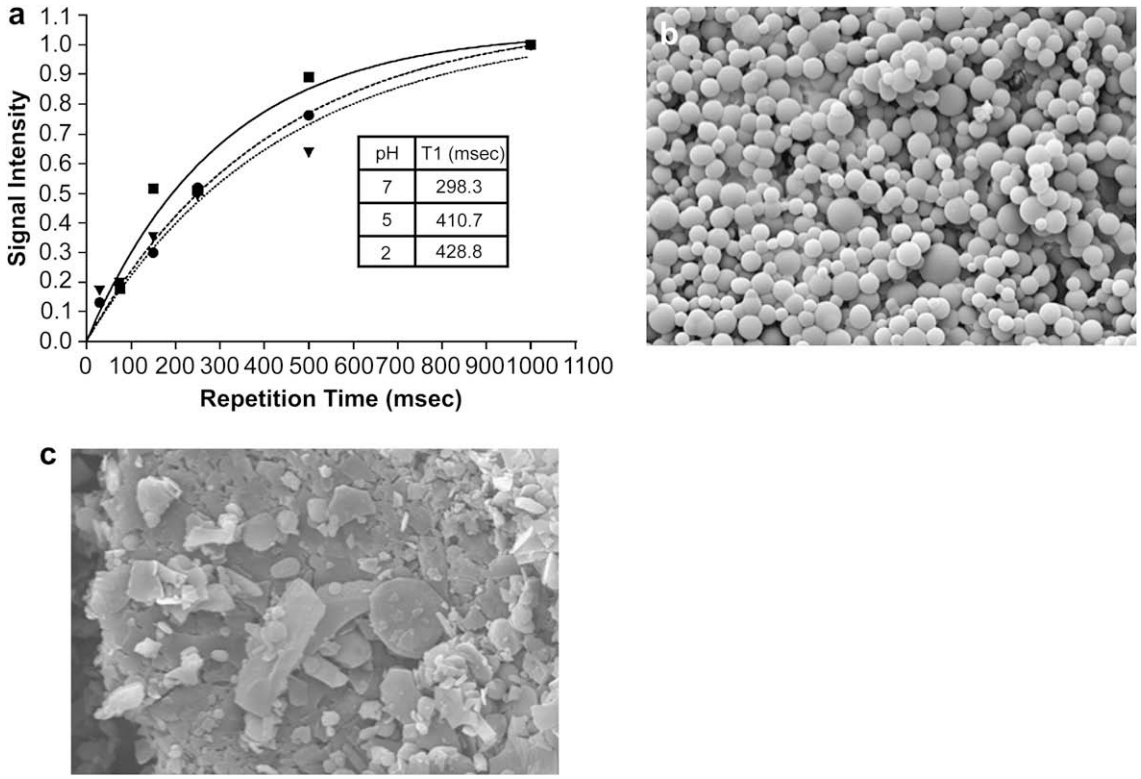


**Fig. 8.** Fate of the fluorinated PAMAM(G3) particulates following exposure to low pH compartments. (a) pH-dependence of *T*1 relaxation times observed by $^{19}F$ magnetic resonance spectroscopy indicate a stable, rigid fluorine network within the particulate at physiological pH that is disrupted at low pH. -▼- represents pH 2.0, -●- represents pH 5.0, and -■- represents pH 7.0. (b) Scanning electron micrograph of fluorinated PAMAM(G3) particulates. (c) Scanning electron micrograph of fluorinated PAMAM(G3) particulates following treatment with 20 mM citrate buffer at pH 2 and subsequent dialysis against water. Particulate disassembly was observed to be irreversible. Scale bar is 10 μm.

is disrupted upon exposure to low pH environments. This observation was confirmed by SEM (Fig. 8b and c).

## 4. Conclusions

Covalent attachment of perfluoroalkyl substituents to the surface of PAMAM dendrimers mediates self-assembly into a complex system with unique and adjustable physiochemical properties. Self-assembly by partial fluorination of nanoscale dendrimer units preserves dendrimer features that are important for biomedical applications, while introducing new functionalities. A distinct feature of this system is the intrinsic imaging component that enables noninvasive monitoring of particulate trafficking *in vivo*. Further, the stimulus-induced response to subtle changes in pH makes possible targeting drug to or imaging capabilities of low pH physiological compartments.

## Acknowledgements

The authors would like to thank Alec Flyer for assistance with the synthesis design; Dr. Pavel Shkarin for assistance with the imaging; Dr. Zhenting Jiang for his assistance with SEM; Dr. Paul van Tassel and Dr. Fred Sigworth for their intellectual contributions to the work and careful reading of the manuscript; Lauren Criscione for graphic design.

## Appendix. Supplementary data

Supplementary data associated with this article can be found in the on-line version at doi:10.1016/j.biomaterials.2009.04.014.

## Appendix

Figures with essential colour discrimination. Parts of Figs. 6 and 7 of this article are difficult to interpret in black and white. The full colour images can be found in the on-line version, at doi:10.1016/j.biomaterials.2009.04.014.

## References

[1] Svenson S, Tomalia D. Dendrimers in biomedical applications-reflections on the field. Adv Drug Deliv Rev 2005;57(15):2106–29.
[2] Tomalia DA, Naylor AM, Goddard III WA. Starburst dendrimers: molecular-level control of size, shape, surface chemistry, topology, and flexibility from atoms to macroscopic matter. Angew Chem Int Ed 1990;29:138–75.
[3] Tomalia DA, Reyna LA, Svenson S. Dendrimers as multi-purpose nanodevices for oncology drug delivery and diagnostic imaging. Biochem Soc Trans 2007;35:61–7.
[4] Venditto VJ, Regino CA, Brechbiel MW. PAMAM dendrimer based macromolecules as improved contrast agents. Mol Pharmacol 2005;2(4):302–11.
[5] Wiener EC, Brechbiel MW, Brothers H, Magin RL, Gansow OA, Tomalia DA, et al. Dendrimer-based metal chelates: a new class of magnetic resonance imaging contrast agents. Magn Reson Med 1994;31(1):1–8.
[6] Xu S, Kramer M, Haag R. pH-responsive dendritic core–shell architectures as amphiphilic nanocarriers for polar drugs. J Drug Target 2006;14(6):367–74.
[7] Patri AK, Kukowska-Latallo JF, Baker Jr JR. Targeted drug delivery with dendrimers: comparison of the release kinetics of covalently conjugated drug and non-covalent drug inclusion complex. Adv Drug Deliv Rev 2005;57(15):2203–14.
[8] Mounzer R, Shkarin P, Papademetris X, Constable T, Ruddle N, Fahmy T. Dynamic imaging of lymphatic vessels and lymph nodes using a bimodal nanoparticulate contrast agent. Lymphat Res and Biol 2007;5(3):151–8.
[9] Kobayashi H, Brechbiel M. Nano-sized MRI contrast agents with dendrimer cores. Adv Drug Deliv Rev 2005;57(15):2271–86.
[10] Kobayashi H, Brechbiel MW. Dendrimer-based macromolecular MRI contrast agents: characteristics and application. Mol Imaging 2003;2(1):1–10.
[11] Kobayashi H, Brechbiel MW. Dendrimer-based nanosized MRI contrast agents. Curr Pharm Biotechnol 2004;5(6):539–49.
[12] Talanov VS, Regino CA, Kobayashi H, Bernardo M, Choyke PL, Brechbiel MW. Dendrimer-based nanoprobe for dual modality magnetic resonance and fluorescence imaging. Nano Lett 2006;6(7):1459–63.
[13] Jászberényi Z, Moriggi L, Schmidt P, Weidensteiner C, Kneuer R, Merbach A, et al. Physicochemical and MRI characterization of Gd3+-loaded polyamidoamine and hyperbranched dendrimers. J Biol Inorg Chem 2007;12(3):406–20.
[14] Fahmy T, Schneck J, Saltzman W. A nanoscopic multivalent antigen-presenting carrier for sensitive detection and drug delivery to T cells. Nanomedicine 2007;3(1):75–85.
[15] Bielinska AU, Chen C, Johnson J, Baker Jr JR. DNA complexing with polyamidoamine dendrimers: implications for transfection. Bioconjug Chem 1999;10(5):843–50.
[16] Uchiyama T, Ishii K, Nonomura T, Kobayashi N, Isoda S. A phthalocyanine dendrimer capable of forming spherical micelles. Chemistry 2003;9(23):5757–61.
[17] Percec V, Glodde M, Johansson G, Balagurusamy V, Heiney P. Transformation of a spherical supramolecular dendrimer into a pyramidal columnar supramolecular dendrimer mediated by the fluorophobic effect. Angew Chem Int Ed 2003;115(36):4474–8.
[18] Percec V, Johansson G, Ungar G, Zhou JP. Fluorophobic effect induces the self-assembly of semifluorinated tapered monodendrons containing crown ethers into supramolecular columnar dendrimers which exhibit a homeotropic hexagonal columnar liquid crystalline phase. J Am Chem Soc 1996;118(41):9855–66.
[19] Corbin PS, Lawless LJ, Li Z, Ma Y, Witmer MJ, Zimmerman SC. Discrete and polymeric self-assembled dendrimers: hydrogen bond-mediated assembly with high stability and high fidelity. Proc Natl Acad Sci U S A 2002;99(8):5099–104.
[20] Zimmerman SC, Zeng F, Reichert DE, Kolotuchin SV. Self-assembling dendrimers. Science 1996;271(5252):1095–8.
[21] Wang Y, Zeng FW, Zimmerman SC. Dendrimers with anthyridine-based hydrogen-bonding units at their cores: synthesis, complexation and self-assembly studies. Tetrahedron Lett 1997;38:5459–62.
[22] Jeong KS, Park EJ. Self-assembly of interlocked supramolecular dendrimers. J Org Chem 2004;69(7):2618–21.
[23] Kawa M, Frechet JMJ. Self-assembled lanthanide-cored dendrimer complexes: enhancement of the luminescence properties of lanthanide ions through site-isolation and antenna effects. Chem Mater 1998;10(1):286–96.
[24] Issberner J, Vogtle F, DeCola L, Balzani V. Dendritic bipyridine ligands and their tris(bipyridine)ruthenium(II) chelates – syntheses, absorption spectra, and photophysical properties. Chem Eur J 1997;3(5):706–12.
[25] Martin OM, Yu L, Mecozzi S. Solution self-assembly and solid state properties of fluorinated amphiphilic calix [4]arenes. Chem Commun 2005;39:4964–6.
[26] Hunter R. Foundations of colloid science. 2nd ed. New York: Oxford University Press, Inc.; 2001.
[27] Kimura A, Narazaki M, Kanazawa Y, Fujiwara H. $^{19}F$ magnetic resonance imaging of perfluorooctanoic acid encapsulated in liposome for biodistribution measurement. Magn Reson Imaging 2004;22(6):855–60.
[28] Ahrens E, Flores R, Xu H, Morel P. In vivo imaging platform for tracking immunotherapeutic cells. Nat Biotechnol 2005;23(8):983–7.
[29] Janjic JM, Srinivas M, Kadayakkara DKK, Ahrens E. Self-delivering nanoemulsions for dual fluorine-19 MRI and fluorescence detection. J Am Chem Soc 2008;130(9):2832–41.
[30] Caruthers SD, Neubauer AM, Hockett FD, Lamerichs R, Winter PM, Scott MJ, et al. In vitro demonstration using $^{19}F$ magnetic resonance to augment molecular imaging with paramagnetic perfluorocarbon nanoparticles at 1.5 T. Invest Radiol 2006;41(3):305–12.
[31] Lanza G, Winter P, Neubauer A, Caruthers S, Hockett F, Wickline S. $^{1}H/^{19}F$ magnetic resonance molecular imaging with perfluorocarbon nanoparticles. Curr Top Dev Biol 2005;70:57–76.
[32] Partlow K, Chen J, Brant J, Neubauer A, Meyerrose T, Creer M, et al. 19F magnetic resonance imaging for stem/progenitor cell tracking with multiple unique perfluorocarbon nanobeacons. FASEB J 2007;21(8):1647–54.
[33] Srinivas M, Morel P, Ernst L, Laidlaw D, Ahrens E. Fluorine-19 MRI for visualization and quantification of cell migration in a diabetes model. Magn Reson Med 2007;58(4):725–34.
[34] Morawski A, Winter P, Yu X, Fuhrhop R, Scott M, Hockett F, et al. Quantitative magnetic resonance immunohistochemistry with ligand-targeted19F nanoparticles. Magn Reson Med 2004;52(6):1255–62.
[35] Pykett IL, Rosen BR. Nuclear magnetic resonance: in vivo proton chemical shift imaging. Radiology 1983;149:197–201.
[36] Katre N. The conjugation of proteins with polyethylene glycol and other polymers – altering properties of proteins to enhance their therapeutic potential. Adv Drug Deliv Rev 1993;10:91–114.
[37] Papademetris X, Jackowski M, Rajeevan N, Constable RT, Staib LH. BioImage suite: an integrated medical image analysis suite. Online. 2007. Available from URL, http://www.bioimagesuite.org.